Journal of Materials Chemistry

Cite this: J. Mater. Chem., 2012, 22, 10704

www.rsc.org/materials

PAPER

High-performance indium phosphide nanowires synthesized on amorphous substrates: from formation mechanism to optical and electrical transport measurements†

Alvin T. Hui,‡[a] Fengyun Wang,‡[b] Ning Han,[a] SenPo Yip,[a] Fei Xiu,[a] Jared J. Hou,[a] Yu-Ting Yen,[c] TakFu Hung,[a] Yu-Lun Chueh[c] and Johnny C. Ho*[a]

Received 28th February 2012, Accepted 15th March 2012
DOI: 10.1039/c2jm31232h

InP NWs have been extensively explored for next-generation electronic and optoelectronic devices due to their excellent carrier mobility, exciton lifetime and wave-guiding characteristics. Typically, those NWs are grown epitaxially on crystalline substrates which could limit their potential applications requiring high growth yield to be printable or transferable on amorphous and flexible substrates. Here, utilizing Au as catalytic seeds, we successfully demonstrate the synthesis of crystalline, stoichiometric and dense InP NWs on amorphous substrates. Notably, the NWs are found to grow *via* the vapor–liquid–solid (VLS) mechanism with a narrow distribution of diameter (34.6 ± 7.7 nm) uniformly along the entire NW length (>10 μm). Although the grown NWs possess a substantial amount of twin defects, the fabricated NW FETs still exhibit impressive electrical performance with high carrier mobility (~350 $cm^2\ V^{-1}\ s^{-1}$) and I_{ON}/I_{OFF} ratio (~10^6). All these have demonstrated the promising potency of such NWs grown on amorphous substrates for technological applications, as compared to the conventional MBE or MOCVD grown InP NWs.

Introduction

In recent years, due to superior physical properties such as the excellent carrier mobility,[1] exciton lifetime[1] and wave-guiding characteristics,[2] indium phosphide (InP) nanowires (NWs) have been studied extensively as the one-dimensional (1-D) building blocks for future electronics and optoelectronics.[1–6] Several different methods have been utilized to prepare single-crystalline 1-D InP nanostructures, including the top-down etching approach,[7] bottom-up metal–organic chemical vapor deposition (MOCVD),[8] molecular beam epitaxy (MBE)[9] and chemical beam epitaxy (CBE).[10] Among those, NW growth on crystalline substrates by MOCVD and epitaxial methods is typically adopted following the well-known vapor–liquid–solid (VLS) or vapor–solid–solid (VSS) growth mechanism. However, the employment of such crystalline substrates (*e.g.* InP[8] and Si[11]) as the underlying templates could result in the relatively low growth yield of NWs and greatly restrict the subsequent device integration for certain applications.[12] For example, various kinds of NWs have been successfully printed on many receiver substrates, including flexible plastics, for high-performance sensors and electronics.[13,14] In this regard, there is a crucial need to investigate alternative methods of synthesizing high growth yield and single-crystalline InP NWs on non-crystalline substrates, with detailed characterization, for potential technological applications.[15,16] Moreover, a deep understanding of the growth mechanism on amorphous substrates is also of profound interest to further enhance the physical properties of InP NWs.

Here, we demonstrated a successful and facile synthesis method utilizing gold nano-clusters (Au NCs) as the catalysts to achieve high density InP NWs on amorphous Si/SiO_2 substrates *via* solid-source chemical vapor deposition (CVD). The obtained NWs are very uniform in diameter, stoichiometric, crystalline with a smooth surface and are found to follow the VLS mechanism. Although the NWs are grown with zincblende (ZB) crystal structure with significant twin defects and intermixing with a small amount of the wurtzite (WZ) phase, more importantly, they still exhibit the excellent electrical performance when configured as FETs, with the peak field-effect carrier mobility

[a]*Department of Physics and Materials Science, City University of Hong Kong, 83 Tat Chee Ave., H.K. SAR, China. E-mail: johnnyho@cityu.edu.hk; Fax: +852-34420538; Tel: +852-34424897*
[b]*Department of Biology and Chemistry, City University of Hong Kong, 83 Tat Chee Ave., H.K. SAR, China*
[c]*Department of Materials Science & Engineering, National Tsing Hua University, No. 101, Sec. 2 Kuang-Fu Road, Hsinchu 30013, Taiwan*

† Electronic supplementary information (ESI) available: Fig. S1: diameter distribution of 102 individual NWs observed in the TEM images; Fig. S2: (a) HRTEM image of InP NW, same as Fig. 2a (scale bar = 5 nm). (b and d) FFT images of the separated twin segments as marked in (a). The zone axes of (b) and (d) are indexed as $[0\bar{1}\bar{1}]$ and [011] respectively. (c) Enlarged HRTEM image of the WZ phase segment. The zone axis is marked as $[2\bar{1}\bar{1}0]$. See DOI: 10.1039/c2jm31232h

‡ These authors contributed equally to this work.

($\sim$350 $cm^2 V^{-1} s^{-1}$) comparable to the best results reported by the MBE and MOCVD techniques.

Experimental details

Synthesis of InP nanowires

The InP NWs were synthesized on amorphous Si/SiO_2 (50 nm thermally grown) substrates *via* the CVD method. At first, a 0.5 nm thick Au thin film was thermally evaporated onto the pre-cleaned substrate (by ultra-sonication in acetone and then ethanol for 15 minutes each). Next, the growth of InP NWs was carried out in a dual-zone horizontal tube furnace. Solid InP powder (99.995% purity) was placed in a boron nitride (BN) crucible positioned in the up-stream zone while the substrate was placed in the downstream zone with a horizontal tilt angle of $\sim$20° and $\sim$10 cm apart from the source crucible. During the NW growth, the Au coated substrate was first thermally annealed at 800 °C for 10 min in H_2 environment (99.995% purity) with the process pressure of $\sim$0.6 Torr to obtain Au NCs which acted as catalysts for the subsequent growth, similar to the techniques reported in ref. 12,17,18. After that, the source was heated to the temperature of 750–770 °C to allow the vaporization of InP powder and the substrate was set to the growth temperature of 440–480 °C. H_2 flow was kept from 100 to 400 sccm and acted as the carrier gas to transport the precursor vapor to the downstream growth substrate. At the end, the heaters of both source and substrate zones were stopped simultaneously and allowed to cool down to the room temperature under hydrogen flow.

Characterization of InP nanowires

The morphologies of InP NWs were observed by a field-emission scanning electron microscope (FESEM, FEI/Philips XL30) and a transmission electron microscope (TEM, Philips CM-20). The crystal structures were determined by studying the images and reciprocal lattice spots extracted from the Fast Fourier Transform (FFT) with a high-resolution transmission electron microscope (HRTEM, JEOL 2100F). The chemical composition of grown NWs was investigated by the energy dispersive X-ray (EDX) detector attached to the JEOL 2100F.

The optical properties of grown NWs were studied by the micro-photoluminescence (μPL) measurement. The excitation wavelength and power density used were 632.8 nm and 17 000 W m^{-2}, respectively. The luminescence signal was detected by a liquid-nitrogen-cooled charged couple device (CCD). Regarding the assessment of electrical properties, the back-gated single nanowire FETs were studied and fabricated by drop-casting the NW suspension (in ethanol) onto highly doped p-type Si substrates with a 50 nm thermally grown SiO_2 layer as the gate dielectric. Photolithography was then performed to define the source and drain electrodes with the 50 nm thick nickel (Ni) deposited by thermal evaporation under the high-vacuum condition (<2×10^{-6} Torr). The lift-off process was followed to obtain the fabricated FETs. Finally, the electrical properties of the NW FETs were characterized with a standard probe station and semiconductor parameter analyzer (Agilent 4155C).

Results and discussion

Morphology and crystal structure

In the NW synthesis, it is well known that the substrate temperature, V/III ratio and growth pressure are the critical parameters to control the NW growth. In our technique, since the solid source is used, the V/III ratio can mainly be controlled by the source temperature and growth time.[12] After a detailed growth investigation in those process parameters, as shown in Fig. 1a, relatively dense and long (>10 μm) InP NWs were successfully obtained with the source and substrate temperatures of 770 and 460 °C, respectively, H_2 gas flow of 100 sccm, growth pressure of $\sim$0.6 Torr and growth time of 60 minutes. With this optimized growth condition, the TEM image (Fig. 1b) reveals that the grown NWs are relatively straight and smooth, with a native amorphous oxide of $\sim$3 to 4 nm; importantly, there is no tapering observed in the NWs and the diameters are very uniform along the entire length of NWs. Based on the statistics of more than 100 individual NWs studied from the TEM images, the obtained NWs have an average diameter of 34.6 ± 7.7 nm (with the amorphous oxide layer, see Fig. S1†), which is comparable to the variation of commercially available colloidal Au NCs for growing small diameter NWs ($\sim$10 to 15%). To further evaluate the crystal quality of the grown NWs, HRTEM of a representative NW is performed and depicted in Fig. 1c. Combining with the FFT image (Fig. 1c, inset), the obtained NWs exhibit good crystallinity and preferential growth in ⟨111⟩ direction. This is expected due to the low index planes that consist of lower surface energy which favor the crystal growth during the formation of NWs.[19,20] Moreover, the distances between the adjacent lattice planes are found to be 0.34 and 0.29 nm, which are in good agreement with the plane spacings of {111} and {200} equivalent planes in the zincblende (ZB)

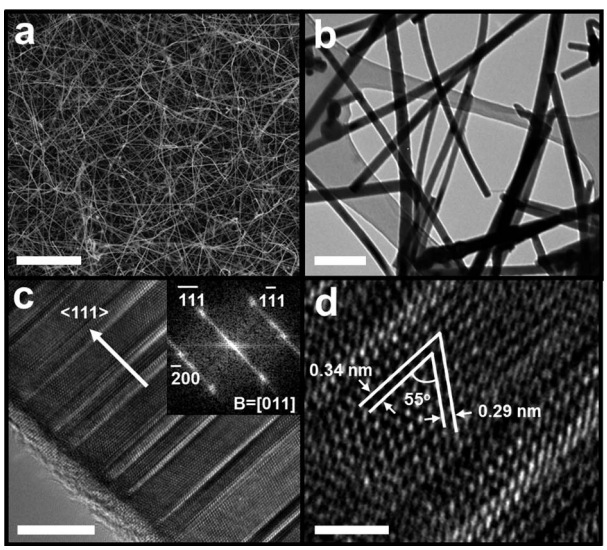

Fig. 1 (a) SEM images of high-density InP NWs (scale bar = 3 μm). (b) TEM image of InP NWs (scale bar = 200 nm). (c) HRTEM image of representative portion of a single NW (scale bar = 10 nm). The thickness of the amorphous layer is about 3 nm. (d) Magnified HRTEM image of the selected region in (c) (scale bar = 2 nm). The lattice plane spacing of adjacent ⟨111⟩ and ⟨200⟩ planes is 0.34 and 0.29 nm, respectively.

structure, respectively. All these factors suggest that the grown NWs are dense with high growth yield, in remarkably narrow diameter distribution and highly crystalline considering the simplicity of this growth technique as contrasted to the sophisticated MBE and MOCVD systems.[9,21]

Phase purity

As shown in Fig. 1c, there are interfaces or boundaries of contrasting segments normal to the NW growth axis, which are commonly observed among the grown NWs. To further shed light on the origin of these segments, various segments are studied thoroughly in Fig. 2a. Specifically, Fast Fourier Transform (FFT) of the example segments of b, c and d was performed. Typical reciprocal lattice spots of normal ZB structure and rotated ZB structure are observed with the zone axis of $[0\bar{1}\bar{1}]$ and [011], respectively (Fig. 2b–d). By studying the atomic stacking of such consecutive segments, the majority of them are in the defects of rotational twins. Therefore, it is believed that the grown NWs are mainly composed of a ZB crystal phase with a high density of twin planes ($\sim$400 μm^{-1}). As reported in the literature, dense twin planes along the $\langle 111 \rangle$ growth direction are common in ZB III–V NWs.[19,20,22] The prevalence of twin planes can be explained by nucleation kinetics[19,23] that the NW growth is in a layer-by-layer mode with a single nucleation event at the edge of the particle–wire interface. Thus, the orientation of each critical nucleus determines whether a normal or a twin plane will be formed. As the energy difference between the normal and twin nuclei is small, small energy fluctuations during growth could give rise to randomly distributed twin planes. This also explains the non-uniformity of segment length throughout the NW. The literature also correlates the single ZB segment length between two coherent twin planes to the NW diameter,[22] while experimental data show that small NW diameter results in the short single segment (<5 nm). The short segment length and high twin-plane density observed in our NW can be probably attributed to the small NW diameter. In addition to the rotational twins, a small number of WZ phase segments have been found in the NWs and form a phase inversion boundary with neighboring ZB segments (see Fig. S2†). Nevertheless, the twin dislocation and phase purity could be further controlled and engineered by fine tuning the NW growth conditions such as the growth temperatures and implementing the post-growth annealing; more detailed investigation is currently in process.

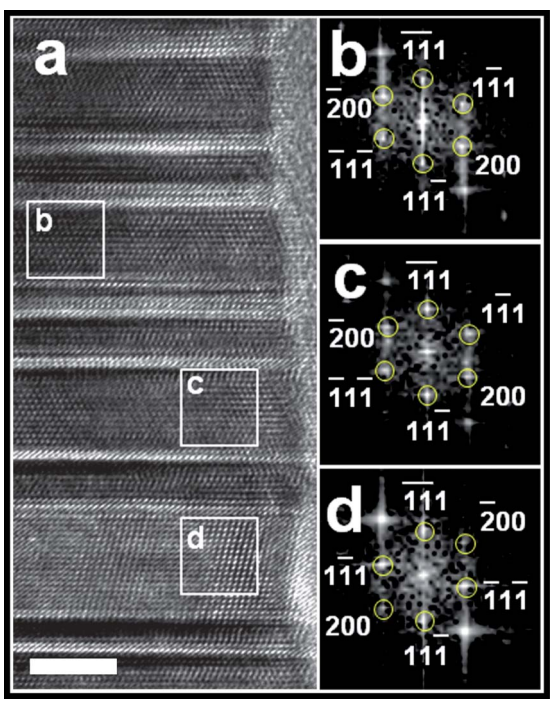

Fig. 2 (a) HRTEM image of a representative InP NW (scale bar = 5 nm). (b–d) FFT reciprocal lattice spots of the selected twin segments as marked in (a). The zone axes of (b) and (c) are indexed as $[0\bar{1}\bar{1}]$ while that of (d) is [011].

Growth mechanism and stoichiometry

To further study the NW formation, as shown in Fig. 3a, the Au-based catalytic seeds are clearly observed at the tips of most NWs, which is the distinct characteristic of the tip-lead VLS/VSS growth mechanism. EDX elemental analysis is also performed on the catalytic seed (region b) and the NW body (region c) to access the corresponding chemical composition. Based on the EDX

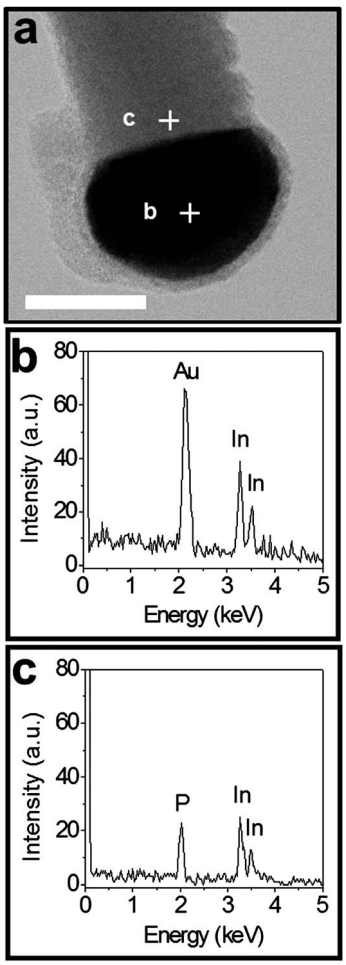

Fig. 3 (a) HRTEM image of InP NW with an Au catalyst (scale bar = 20 nm). (b) and (c) EDX spectra of catalyst tip and NW body respectively.

spectrum illustrated in Fig. 3b, the catalytic seed is only composed of Au and In with atomic ratio of approximately 1 : 1, while no P is found in this region. This suggests that a stable AuIn alloy catalyzes the growth *via* the VLS/VSS mechanism. According to the binary phase diagram of Au and In, the melting point of bulk AuIn is about 450 °C[24] and under the nano-size effect (~35 nm) and low pressure condition, the melting point of the AuIn alloy would be further reduced.[25] In this regard, the AuIn alloy catalyst is believed to exist in liquid phase at the growth temperature (460 °C). The spherical shape of observed catalytic seeds also provides further evidence of the molten catalyst in liquid state. Therefore, the VLS growth mechanism is presumed in our synthesis. As for the mechanism of P incorporation, P probably reacts with In at the catalyst–NW interface rather than dissolving in the catalyst or alloying with the AuIn NCs due to its relatively low solubility in Au.[26] This also explains the absence of the P feature peak in the EDX spectrum in the catalyst region (Fig. 3b). From Fig. 3c, the EDX spectrum reveals that the atomic ratio of In : P is 1 : 1 in the NW body region indicating that the InP NWs are stoichiometric. This balanced stoichiometry is important for achieving good performance of NW electrical devices.[17,27]

As shown in Fig. 4, micro-photoluminescence (μPL) measurement is performed on the NWs drop-casted on the Si/SiO_2 substrate in order to assess the optical properties of our InP NWs. From the PL spectrum, the observed peak is located at ~820 nm (1.5 eV) which is significantly different from the bulk ZB InP PL of ~925 nm (1.34 eV). This blue-shift (~0.16 eV) is mainly due to the quantum confinement size effect which is commonly observed in InP NWs, with the shift correlated well with the average diameter of our grown NWs.[28,29] More importantly, the full width at half maximum (FWHM) of the PL peak is ~165 nm (by Gaussian fit), which is comparable to the value reported in the literature.[4] This relatively large FWHM could be contributed from the diameter variation of NWs, excited under the laser spot, in which different NWs possess different degrees of quantum confinement. Another origin of this broadening is probably attributed to the presence of both ZB and WZ (small amount) phases of InP where their bandgap energy differs by 80–90 meV revealed by both theory[30–32] and experiment.[33]

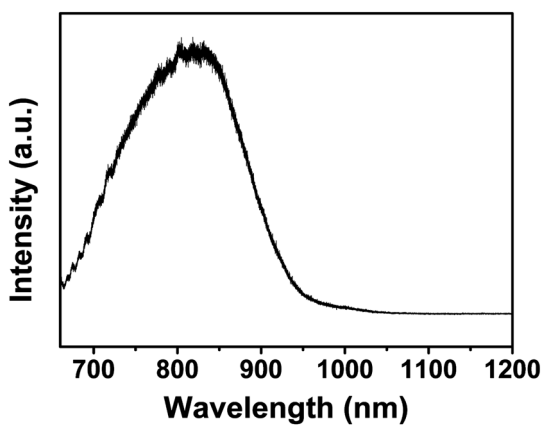

Fig. 4 Room temperature micro-PL of InP NWs on a Si/SiO_2 growth substrate.

Electrical characteristics and performance

To characterize the electrical properties of our InP NWs, single nanowire FETs were fabricated with the common back-gated configuration (~50 nm Ni as the source/drain metal contacts, 50 nm thermally grown oxide as the gate dielectric and heavily boron-doped Si substrate as the bottom-gate). Fig. 5a illustrates the top view SEM image and schematic of the representative FET with NW diameter of ~40 nm and a channel length of 2.2 μm. The corresponding transfer and output characteristics are shown in Fig. 5b and c, respectively. As shown in Fig. 5b, the transistor exhibits n-type conductivity with a minimal hysteresis. A relatively high ON current of 17 μA at V_{DS} of 2.4 V and V_{GS} of 10 V is recorded. The effective carrier concentration can be estimated from the total charge in the NW, $n_e = Q_{tot}/(q\pi r^2 L) = C_{ox}|V_{th}|/(q\pi r^2 L)$, where r is the NW radius, L is the channel length, C_{ox} is the gate capacitance and V_{th} is the threshold voltage. In this case, the capacitance $C_{ox} = 0.12$ fF is obtained from modelling using the finite element analysis software COMSOL for the NW diameter of 32 nm (without the amorphous oxide layer), the channel length of 2.2 μm and the threshold voltage of −5 V. The electron carrier concentration is then estimated to be ~2.3×10^{18} cm^{-3}, which is slightly higher than the undoped NWs grown on crystalline substrates (~10^{17} cm^{-3})[11] and their thin film counterparts (~10^{16} cm^{-3}).[34] Along with the n-type conduction characteristics, all these could be attributed to the unintentional doping of residual impurities arising from our simplified growth system setup as well as the native donor-like defects such as P vacancy.[34,35] From the output characteristics (Fig. 5c), the sub-threshold region at small V_{DS} is not perfectly linear suggesting that the electrical contact of InP NW with Ni electrodes still exhibits Schottky-like behavior. In the future, other contact electrodes such as Ti/Al followed by rapid thermal annealing in forming gas could be adopted to obtain near-Ohmic contact due to the formation of a Ti–P compound.[3,36]

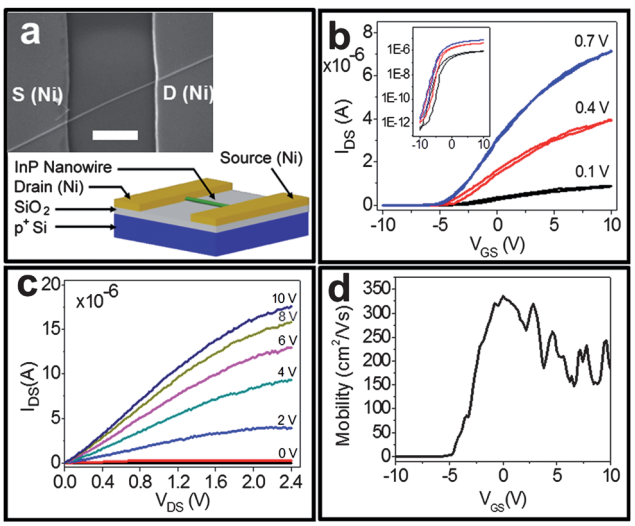

Fig. 5 (a) SEM image and schematic view of the back-gated SNW FET (scale bar = 1 μm). (b) Device transfer characteristic of InP SNW FET shown in (a) with different V_{DS}. (c) Device output characteristics of the same NW device at different V_{GS}. The bottom curve is measured at $V_{GS} = -2$ V. (d) Electron mobility against V_{GS} estimated from the transfer characteristic at $V_{DS} = 0.1$ V using the square-law model.

In order to further shed light to evaluate the NW FET performance, electron mobility is an important figure of merit to relate the drift velocity of electrons to an applied electric field. The mobility can then be estimated from the transfer characteristics and is depicted in Fig. 5d as a function of the back-gate voltage V_{GS}. In this study, the mobility is deduced from the low-bias (V_{DS} = 0.1 V) transconductance, $G_m = dI_{DS}/dV_{GS}$, of the device by using the standard square-law model, $\mu_n = (G_m L^2)/(C_{ox} V_{DS})$, where μ_n is the field-effect mobility, C_{ox} is the gate capacitance and L is the channel length. Notably, the peak mobility is found to be $\sim$350 $cm^2 V^{-1} s^{-1}$ in which it could be further increased with the growth condition optimization to minimize the formation of twin planes and phase-inversion boundaries in reducing the carrier scattering sites at these boundaries.[37] This reported mobility is still lower than their thin film counterparts, which can be mainly attributed to the enhanced surface scattering arising from the nanowire geometry.[38] In any case, this mobility is already comparable to the best one reported by the MBE and MOCVD techniques.[38,39] It is also important that the fabricated device here displays a respectable I_{ON}/I_{OFF} ratio of 10^6 (shown in Fig. 5b) suggesting the excellent gate coupling and low OFF-state leakage, which further demonstrates the profound potency of our solid-source CVD grown InP NWs for high performance electronic and optoelectronic applications.

Conclusions

In summary, we have demonstrated a simple CVD technique to synthesize high-density and stoichiometric InP NWs on a non-crystalline substrate *via* the VLS growth mechanism with Au NCs as the starting catalyst. Notably, the NWs are grown with uniform diameter and smooth surface without any tapering or over-coating which indicate the ease of process control in this growth technique. Also, μPL measurement shows a significant blue-shifted peak which could be due to the quantum confinement size effect. Although the grown NWs possess a substantial amount of twin defects, the fabricated NW FETs still exhibit impressive electrical performance with high carrier mobility and I_{ON}/I_{OFF} ratio, in which the performance is believed to get further improved by reducing the twin density. All these properties have demonstrated the significant potential implications for future electronic and optoelectronic applications of InP NWs grown on amorphous substrates.

Acknowledgements

This work was financially supported by the City University of Hong Kong (project no. 7002597 and 9610180). YLC would like to thank the support from National Science Council of Taiwan through grant no: NSC 98-2112-M-007-025-MY3.

Notes and references

1 X. F. Duan, Y. Huang, Y. Cui, J. F. Wang and C. M. Lieber, *Nature*, 2001, **409**, 66–69.
2 Y. Ding, J. Motohisa, B. Hua, S. Hara and T. Fukui, *Nano Lett.*, 2007, **7**, 3598–3602.
3 S. De Franceschi, J. A. van Dam, E. Bakkers, L. F. Feiner and L. Gurevich, *Appl. Phys. Lett.*, 2003, **83**, 344–346.
4 J. F. Wang, M. S. Gudiksen, X. F. Duan, Y. Cui and C. M. Lieber, *Science*, 2001, **293**, 1455–1457.
5 E. D. Minot, F. Kelkensberg, M. van Kouwen, J. A. van Dam, L. P. Kouwenhoven, V. Zwiller, M. T. Borgstrom, O. Wunnicke, M. A. Verheijen and E. P. A. M. Bakkers, *Nano Lett.*, 2007, **7**, 367–371.
6 X. Jiang, Q. Xiong, S. Nam, F. Qian, Y. Li and C. M. Lieber, *Nano Lett.*, 2007, **7**, 3214–3218.
7 K. Cho, D. J. Ruebusch, M. H. Lee, J. H. Moon, A. C. Ford, R. Kapadia, K. Takei, O. Ergen and A. Javey, *Appl. Phys. Lett.*, 2011, **98**, 203101.
8 S. Paiman, Q. Gao, H. J. Joyce, Y. Kim, H. H. Tan, C. Jagadish, X. Zhang, Y. Guo and J. Zou, *J. Phys. D: Appl. Phys.*, 2010, **43**, 445402.
9 D. M. Cornet, V. G. M. Mazzetti and R. R. LaPierre, *Appl. Phys. Lett.*, 2007, **90**, 013116.
10 D. Dalacu, A. Kam, D. G. Austing, X. Wu, J. Lapointe, G. C. Aers and P. J. Poole, *Nanotechnology*, 2009, **20**, 395602.
11 C. Liu, L. Dai, L. P. You, W. J. Xu and G. G. Qin, *Nanotechnology*, 2008, **19**, 465203.
12 N. Han, F. Wang, A. T. Hui, J. J. Hou, G. Shan, F. Xiu, T. Hung and J. C. Ho, *Nanotechnology*, 2011, **22**, 083114.
13 K. Takei, T. Takahashi, J. C. Ho, H. Ko, A. G. Gillies, P. W. Leu, R. S. Fearing and A. Javey, *Nat. Mater.*, 2010, **9**, 821–826.
14 Z. Fan, J. C. Ho, Z. A. Jacobson, H. Razavi and A. Javey, *Proc. Natl. Acad. Sci. U. S. A.*, 2008, **105**, 11066–11070.
15 S. A. Fortuna, J. Wen, I. S. Chun and X. Li, *Nano Lett.*, 2008, **8**, 4421–4427.
16 Z. Fan, J. C. Ho, T. Takahashi, R. Yerushalmi, K. Takei, A. C. Ford, Y. L. Chueh and A. Javey, *Adv. Mater.*, 2009, **21**, 3730–3743.
17 A. C. Ford, J. C. Ho, Z. Y. Fan, O. Ergen, V. Altoe, S. Aloni, H. Razavi and A. Javey, *Nano Res.*, 2008, **1**, 32–39.
18 A. C. Ford, J. C. Ho, Y. L. Chueh, Y. C. Tseng, Z. Fan, J. Guo, J. Bokor and A. Javey, *Nano Lett.*, 2009, **9**, 360–365.
19 J. Johansson, L. S. Karlsson, C. P. T. Svensson, T. Martensson, B. A. Wacaser, K. Deppert, L. Samuelson and W. Seifert, *Nat. Mater.*, 2006, **5**, 574–580.
20 K. A. Dick, P. Caroff, J. Bolinsson, M. E. Messing, J. Johansson, K. Deppert, L. R. Wallenberg and L. Samuelson, *Semicond. Sci. Technol.*, 2010, **25**, 024009.
21 M. Moewe, L. C. Chuang, V. G. Dubrovskii and C. Chang-Hasnain, *J. Appl. Phys.*, 2008, **104**, 044313.
22 P. Caroff, K. A. Dick, J. Johansson, M. E. Messing, K. Deppert and L. Samuelson, *Nat. Nanotechnol.*, 2009, **4**, 50–55.
23 F. Glas, J. C. Harmand and G. Patriarche, *Phys. Rev. Lett.*, 2007, **99**, 146101.
24 *Metal Handbook*, ed. T. Lyman, American Society for Metals, Metals Park, OH, 1980, vol. 8.
25 P. Buffat and J.-P. Borel, *Phys. Rev. A: At., Mol., Opt. Phys.*, 1976, **13**, 2287–2298.
26 H. Okamoto and T. B. Massalski, *J. Phase Equilib.*, 1984, **5**, 490–491.
27 A. Klein, F. Säuberlich, B. Späth, T. Schulmeyer and D. Kraft, *J. Mater. Sci.*, 2007, **42**, 1890–1900.
28 M. S. Gudiksen, J. Wang and C. M. Lieber, *J. Phys. Chem. B*, 2002, **106**, 4036–4039.
29 M. Mattila, T. Hakkarainen, M. Mulot and H. Lipsanen, *Nanotechnology*, 2006, **17**, 1580–1583.
30 M. Murayama and T. Nakayama, *Phys. Rev. B: Condens. Matter*, 1994, **49**, 4710–4724.
31 L. Zhang, J. W. Luo, A. Zunger, N. Akopian, V. Zwiller and J. C. Harmand, *Nano Lett.*, 2010, **10**, 4055–4060.
32 T. Akiyama, K. Sano, K. Nakamura and T. Ito, *Jpn. J. Appl. Phys.*, 2006, **45**, 275–278.
33 A. Mishra, L. V. Titova, T. B. Hoang, H. E. Jackson, L. M. Smith, J. M. Yarrison-Rice, Y. Kim, H. J. Joyce, Q. Gao, H. H. Tan and C. Jagadish, *Appl. Phys. Lett.*, 2007, **91**, 263104.
34 G. Hema Chandra, J. Pérez de la Cruz and J. Ventura, *Semicond. Sci. Technol.*, 2011, **26**, 075017.
35 S. A. Stockman, M. T. Fresina, Q. J. Hartmann, A. W. Hanson, N. F. Gardner, J. E. Baker and G. E. Stillman, *J. Appl. Phys.*, 1994, **75**, 4233–4236.
36 M. B. Takeyama, A. Noya, T. Hashizume and H. Hasegawa, *Jpn. J. Appl. Phys.*, 1999, **38**, 1115–1118.
37 M. D. Schroer and J. R. Petta, *Nano Lett.*, 2010, **10**, 1618–1622.
38 M. T. Borgström, E. Norberg, P. Wickert, H. A. Nilsson, J. Trägårdh, K. A. Dick, G. Statkute, P. Ramvall, K. Deppert and L. Samuelson, *Nanotechnology*, 2008, **19**, 445602.
39 K. Storm, G. Nylund, M. Borgström, J. Wallentin, C. Fasth, C. Thelander and L. Samuelson, *Nano Lett.*, 2011, **11**, 1127–1130.

